CEAS Aeronaut J (2018) 9:291–306
https://doi.org/10.1007/s13272-017-0247-2

ORIGINAL PAPER

APIAN-INF: an aerodynamic and aeroacoustic investigation of pylon-interaction effects for pusher propellers

Tomas Sinnige[1] · Daniele Ragni[1] · Anwar M. N. Malgoezar[1] · Georg Eitelberg[1] · Leo L. M. Veldhuis[1]

Received: 30 April 2016 / Revised: 19 April 2017 / Accepted: 15 May 2017 / Published online: 2 June 2017

Abstract Advanced propellers promise significant fuel-burn savings compared to turbofans. When installed on the fuselage in a pusher configuration, the propeller interacts with the wake of the supporting pylon. This paper presents an experimental analysis of the aerodynamic and aeroacoustic characteristics of this pylon–propeller interaction. An isolated propeller was operated in undisturbed flow and in the wake of an upstream pylon at the large low-speed facility of the German–Dutch wind tunnels (DNW-LLF). Measurements of the pylon-wake characteristics showed that the wake width and velocity deficit decreased with increasing thrust due to the suction of the propeller. The installation of the pylon led to a tonal noise penalty of up to 24 dB, resulting from the periodic blade-loading fluctuations caused by the wake encounter. The noise penalty peaked in the upstream direction and became increasingly prominent with decreasing propeller thrust setting, due to the associated reduction of the steady blade loads. The integral propeller performance was not significantly altered by the pylon-wake encounter process. However, at sideslip angles of ±6°, the effective advance ratio of the propeller was modified by the circumferential velocity components induced by the pylon tip vortex. The propeller performance improved when the direction of rotation of the propeller was opposite to that of the pylon tip vortex. Under this condition, a reduction was measured in the noise emissions due to a favorable superposition of the angular-inflow and pylon-wake effects.

This paper is based on a presentation at the CEAS Air & Space Conference 2015, September 7–11, Delft, The Netherlands.

✉ Tomas Sinnige
T.Sinnige@tudelft.nl

[1] Faculty of Aerospace Engineering, Delft University of Technology, Kluyverweg 1, 2629 HS Delft, The Netherlands

Keywords Propulsion integration · Pusher propellers · Propeller noise · Pylon-installation effects

List of symbols

B	Number of blades
BPF	Blade-passage frequency [Hz], $BPF = nB$
c	Pylon chord [m]
c_b	Propeller blade chord [m]
c_n	Sectional blade normal-force coefficient, $c_n = n/(q_{rot}c_b)$
C_p	Pressure coefficient, $C_p = (p - p_\infty)/q_{rot}$
C_Q	Torque coefficient, $C_Q = Q/(\rho_\infty n^2 D^5)$
C_T	Thrust coefficient, $C_T = T/(\rho_\infty n^2 D^4)$
D	Propeller diameter [m]
f	Frequency [Hz]
J	Advance ratio, $J = U_\infty/(nD)$
k	Reduced frequency, $k = \omega c_b/(2U_{rot})$
n	Propeller rotational frequency [Hz]
p	Pressure [Pa]
p_∞	Free-stream static pressure [Pa]
q_{rot}	Local dynamic pressure in rotating frame [Pa], $q_{rot}(r) = 0.5\rho_\infty\left(U_\infty^2 + (2\pi n)^2 r^2\right)$
Q	Torque [Nm]
r	Radial coordinate [m]
R	Propeller radius [m]
SPL	Sound pressure level [dB]
SO	Shaft order, $SO = f/n$
T	Thrust force [N]
U	Axial velocity [m/s]
U_{rot}	Local blade velocity in rotational frame [m/s], $U_{rot}(r) = \sqrt{U_\infty^2 + (2\pi n)^2 r^2}$
U_∞	Free-stream velocity [m/s]
V	Lateral velocity [m/s]

x_b Chordwise coordinate along blade [m]
X Axial coordinate [m]
Y Lateral coordinate [m]
Z Vertical coordinate [m]
β Sideslip angle [deg]
ΔC_T Change in thrust coefficient due to pylon installation
ΔJ_β Change in effective advance ratio for constant propeller thrust due to tip-vortex interaction
ΔX Distance from pylon trailing edge [m]
ϵ Uncertainty of velocity from PIV measurement [m/s]
η Propeller efficiency, $\eta = (J/2\pi)(C_T/C_Q)$
θ Axial directivity angle [deg]
θ_e Axial emission angle [deg]
ρ_∞ Free-stream density [kg/m^3]
ϕ Circumferential directivity angle, blade position [deg]
ω Circular frequency [rad/s]

1 Introduction

Today's concerns about environmental issues together with increasing pressure on airlines' profit margins motivate the need for more fuel-efficient aircraft. In this context, propeller propulsion systems provide an interesting alternative to turbofans. A recent aircraft design study [1] predicted fuel-burn reductions of 10–20% by replacing equivalent-technology-level turbofans with modern propellers. In the last decades, the maximum operating speed of propellers has improved due to modern propeller designs, featuring high disk loadings and swept blades. However, the noise emissions of the propeller still pose a challenge, especially due to the absence of an engine cowling and the relatively high Mach numbers at the blade tip.

To minimize cabin noise, the propellers should be positioned as far away as possible from the passengers. In this regard, the best aircraft configuration features pylon-mounted pusher propellers, installed at the rear of the fuselage [2, 3]. Such a layout brings along additional benefits in terms of ground clearance and slipstream-interference drag when compared to a conventional wing-mounted setup [3]. However, the position of the propeller downstream of its support introduces severe unsteady loading on the propeller disk [4]. This is due to the cyclic passage of the blades through the momentum deficit in the pylon wake, causing a sudden increase in the angle of attack of the blades and a decrease in the local dynamic pressure. The resulting periodic change in the pressure field causes an additional source of tonal noise, next to the noise sources due to blade thickness and steady loading associated with the isolated propeller [5].

Previous experimental work [6–11] focused on the aeroacoustic impact of the pylon-wake impingement for semi-installed pusher propellers. More recently, acoustic investigations were reported that extended the scope to complete aircraft configurations [12, 13]. In all cases, significant tonal noise penalties were measured compared to the isolated propeller test case. Such noise penalties have been observed for both single- and contra-rotating propellers; for the latter, the phenomenon is dominated by the tones emitted by the first blade row [9, 10]. The additional noise due to the pylon-wake interaction is a function of the operating conditions of the propeller. Block [6] showed that the magnitude of the overall tonal noise penalty decreases with increasing tip Mach number or disk loading. Magliozzi [8] presented acoustic data for an installed pusher propeller at an angle of attack and observed that the noise penalty due to the installation of the pylon was larger for the symmetric case than for the configuration in angular inflow. This was attributed to a flow-straightening effect of the pylon. Apart from the increased amplitude of the noise emissions, the installation of the pylon also introduces a shift in the harmonic content of the propeller noise [14]. Additionally, the directivity of the noise emissions is modified due to the pylon-installation effects. The interaction noise penalty is especially pronounced away from the propeller plane, where the noise emissions of the isolated propeller are relatively low [6, 14].

Despite the main source of noise being known, the relation between the pylon–propeller interaction and the propeller performance is still controversial. Among the few existing studies on the topic, Gentry et al. [15] observed a favorable installation effect on the thrust levels of a propeller with an upstream pylon and nacelle. This was, however, attributed to the presence of the nacelle wake, while the effect of the pylon wake was considered negligible. No blade-loading information was available to support this conclusion. Such data were available in the work of Farokhi et al. [4, 17], which showed that the pylon-wake impingement is experienced by the blades as a periodic, impulsive increase in blade loading. Next to the detrimental effects due to the wake encounter, also a beneficial interaction occurs due to tip-vortex recovery. Experiments on a wingtip-mounted pusher propeller highlighted that part of the vortex energy can be recovered by locating the propeller within the tip vortex of the wing [16]. Again, the unsteady propeller blade loads were not considered; hence a complete understanding of the vortex recovery mechanism, including the effects on the propeller noise emissions, remains unavailable.

Numerical work performed by Stürmer [18] confirmed previous findings on the pylon-wake impact on the propeller noise emissions, while additionally discussing the effects of the unsteady blade loads during the wake

encounter. Moreover, a combined experimental–analytical study [19] identified the wake-impingement effect on the propeller noise signatures. Consequently, it is understood that the pylon-wake encounter causes unsteady blade loads and a noise increase. However, no experimental study is available that discusses both simultaneously. The purpose of the current paper is to provide such a comprehensive analysis of the aerodynamic and aeroacoustic interaction effects occurring for pylon-mounted pusher propellers, based on experimental data obtained in a large-scale industrial wind-tunnel facility. Following a characterization of the nonuniform inflow to the propeller due to the pylon wake, the resulting unsteady aerodynamic response of the blades is discussed. The impact of the pylon-wake encounter on the integral propeller performance is then substantiated, after which the aeroacoustic interaction effects are highlighted. The sensitivity of the installation effects to the propeller operating conditions and inflow angle are considered throughout the paper.

2 Experimental setup

Experiments were performed using a setup constituted by a propeller model installed downstream of a pylon, as depicted in Fig. 1. The test campaign was carried out at the Large Low-Speed Facility of the German–Dutch Wind Tunnels (DNW-LLF). The tunnel was operated in its open-jet configuration, with an outlet of 8 m × 6 m. The turbulence intensity in the longitudinal and lateral directions equals 0.24% and 0.13% at the selected free-stream velocity of 60 m/s. Acoustic treatment of the test section allowed for semi-anechoic test conditions.

The characteristics of the propeller and pylon models are provided in Tables 1 and 2, respectively. The six-bladed propeller of 0.508 m diameter was designed and built for the EU-funded APIAN project [20–22]. The blade pitch angle was set to 40.4° at r/R = 0.75, as defined from the direction of the tangential velocity of the blade. The propeller was run at three different conditions: high, intermediate, and low thrust settings, corresponding to thrust-coefficient values C_T of 0.51, 0.36, and 0.18. Since the blade pitch angle was fixed during the tests, the different thrust settings were achieved by changing the propeller rotational speed. The associated advance ratios J equaled 1.05, 1.40, and 1.75, respectively.

The pylon with chord length of 0.489 m featured a straight, unswept planform. The NACA 0010 cross section was modified to obtain a trailing-edge thickness of $0.008c$. This was required to fit a blowing system into the aft part of the model [23]. The current paper only discusses results obtained without application of the blowing system. The leading edge of the propeller blade was positioned at approximately 30% of the propeller diameter downstream of the pylon trailing edge, as depicted in Fig. 2. The pylon–propeller combination was mounted on a fixed support system, which could be rotated around its vertical axis. The system allowed operation at sideslip angles of +6° and −6°, defined positive as in Fig. 3a.

Four propeller blades were instrumented with surface-pressure transducers, featuring a maximum frequency response of approximately 10 kHz. At a radial station of $r/R \approx 0.65$, seven sensors were flush-mounted on both the suction and pressure sides of the blades, at the chordwise coordinates x/c_b = [0.05, 0.15, 0.30, 0.45, 0.60, 0.75, 0.90]. The measurement time per data point was 30 s, corresponding to approximately 2000–3500 propeller revolutions, depending on the rotational speed of the propeller. The effects of calibration drifts were limited by averaging the measurement data over 6–17 repeated runs per operating condition. Spectral analysis was performed on the raw data using Welch's method [24] with 94 blocks, no overlap, and Hann windows, resulting in frequency spectra with a frequency resolution of approximately 3 Hz. Moreover, a one-pulse-per-revolution trigger signal was used as a reference for phase averaging of the recorded data. In addition to the pressure transducers installed in the blades, a rotating shaft balance (RSB) was integrated into the propeller hub to acquire propeller thrust and torque during all runs. Again, a measurement time of 30 s was used, while similar data processing techniques were applied as for the pressure transducers.

To quantify the nonuniformity of the propeller inflow, stereoscopic particle-image velocimetry (sPIV) was employed. Horizontal measurement planes were positioned between the pylon trailing edge and the propeller. An illustration of the measurement-plane locations is provided in Fig. 4. A detailed overview of the data acquisition and postprocessing characteristics of the sPIV setup is provided in Table 3. Fields of view of about 152 mm x 212 mm were centered at the pylon trailing edge in the lateral direction. Six planes were considered, positioned at 0.34, 0.49, 0.69, 0.79, 0.89, and 0.99 times the propeller radius below the propeller axis. For each plane, a total of 330 image pairs were averaged to obtain converged mean flow fields. Postprocessing was performed using an iterative multi-grid method, with final interrogation window size of 24 pixel × 24 pixel and 50% overlap. The uncertainty of the PIV data was estimated taking into account the uncertainty of the cross-correlation of the image pairs, the convergence of the mean, and image disparity. The resulting uncertainty amounted to around 3.6% of the free-stream velocity.

The propeller noise emissions were evaluated using 39 inflow microphones, installed in a wing-shaped support structure. A detailed description of the system is provided

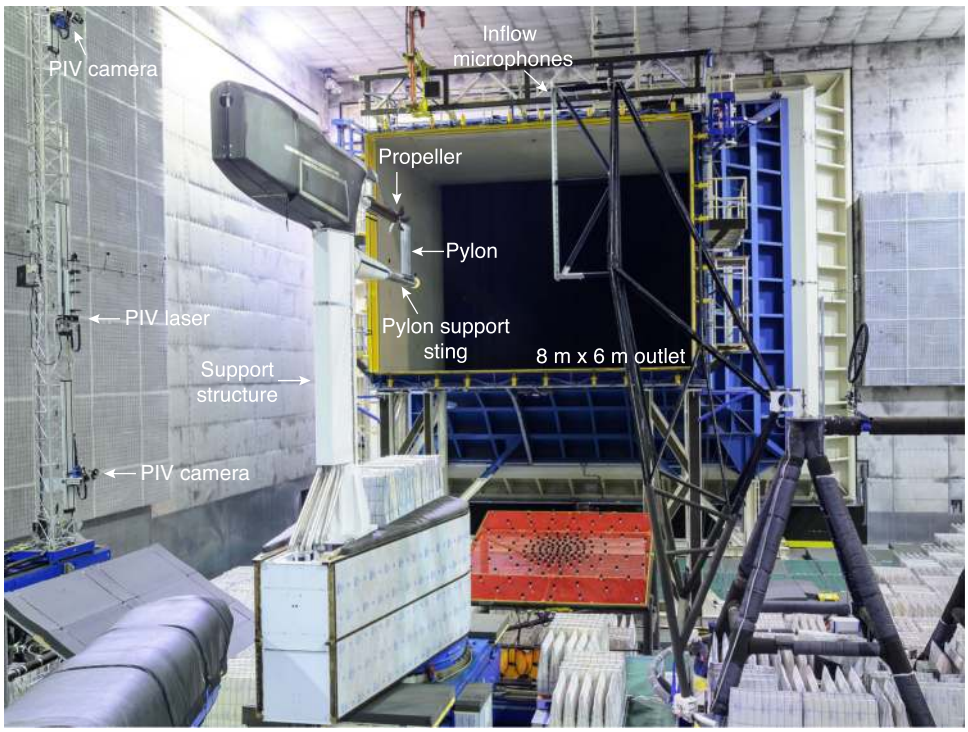

Fig. 1 Photograph of the experimental setup, showing the propeller and pylon models, acoustic instrumentation, and PIV system

Table 1 Propeller model characteristics

Parameter	Value
Diameter	0.508 m
Blade count	6
Blade pitch ($r/R = 0.75$)	40.4°

Table 2 Pylon model characteristics

Parameter	Value
Chord	0.489 m
Span	0.900 m
Taper ratio	0
Sweep angle	0°
Airfoil	NACA 0010
Trailing-edge thickness	0.008c
Pylon–propeller spacing	0.3D

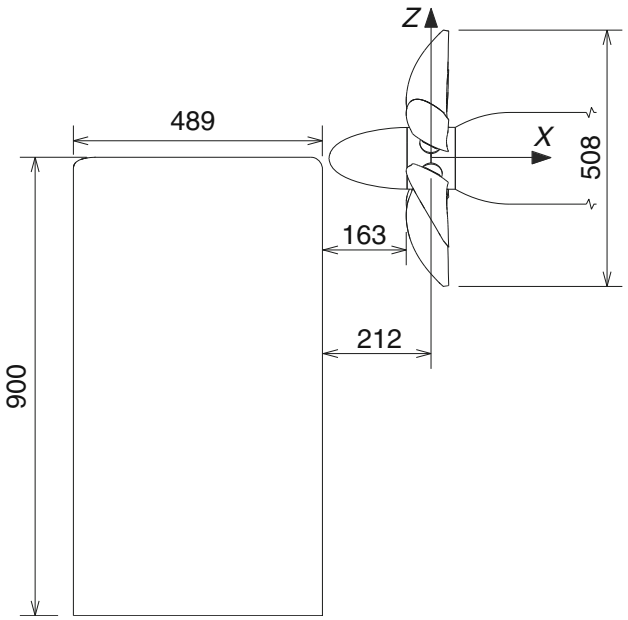

Fig. 2 Geometry of the pylon–propeller combination

in [13]. All microphone data were recorded for a measurement time of 30 s, at a sampling rate of 51.2 kHz. Spectral analysis and phase averaging of the data were performed using the same approach as taken for the pressure-transducer data. To extract the purely harmonic content from the microphone data, bandpass filters were applied around the frequencies corresponding to the first ten multiples of the BPF. In this way, the acoustic signatures were obtained associated with each of the individual propeller tones. The in flow microphone wing was traversed in the axial direction to cover a geometric directivity range of $30° \leq \theta \leq 150°$, as defined at the vertical position of the propeller axis. The corresponding circumferential directivity angle range was $57° \leq \phi \leq 111°$. The definition of the axial and circumferential directivity angles is provided in Fig. 3b, c. The circumferential angle ϕ was also used to refer to the blade position for the aerodynamic measurements.

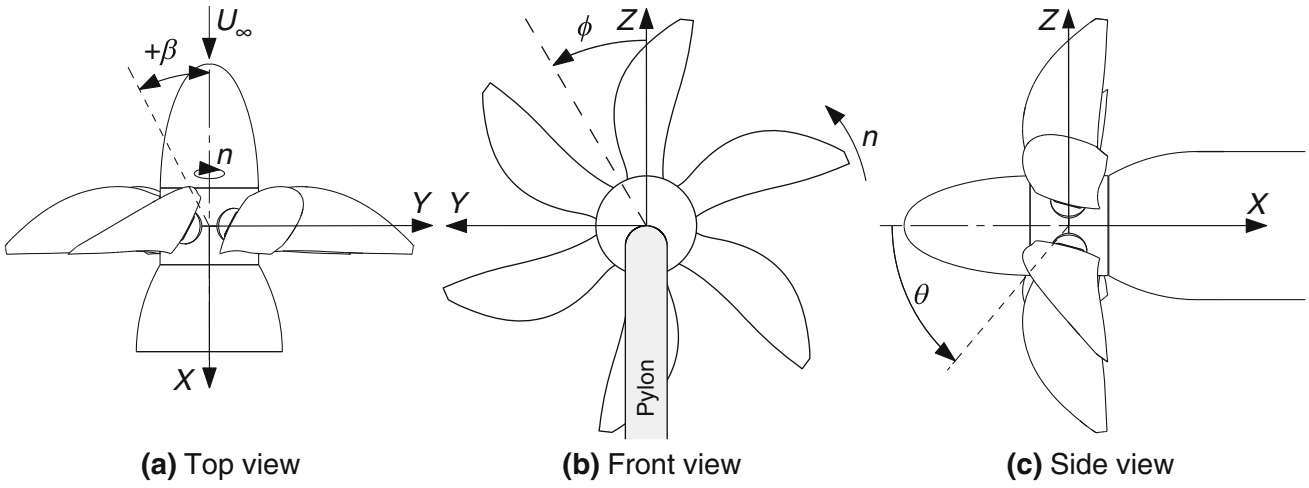

Fig. 3 Definition of reference systems

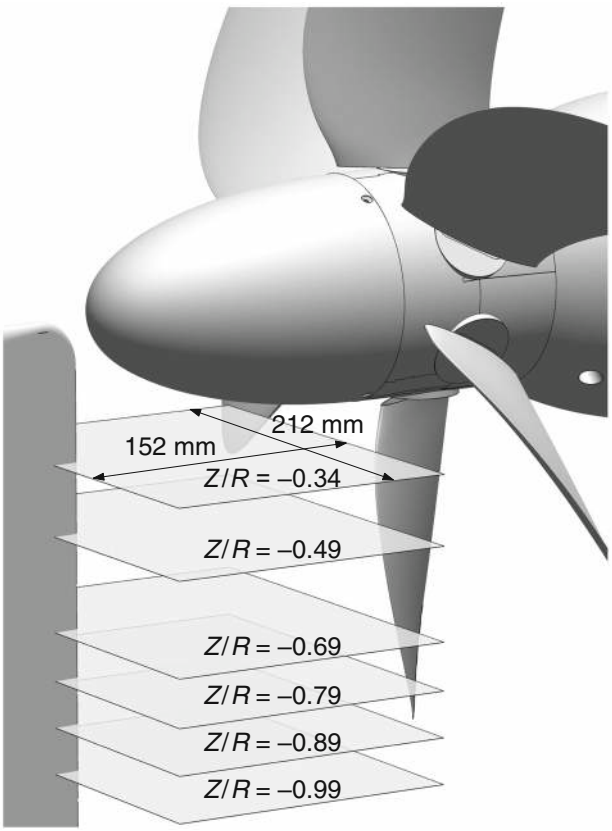

Fig. 4 Illustration of the locations of the sPIV measurement planes

3 Experimental results

3.1 Aerodynamic interaction effects

The installation of the pylon upstream of the propeller introduces two major aerodynamic interactions. This section presents and discusses both: the effects of the propeller on the pylon-wake characteristics and the modification of the propeller blade response by the periodic wake impingement.

3.1.1 Symmetric inflow conditions

The sPIV setup was used to characterize the inflow experienced by the propeller in the pylon-on configuration. Figure 5 provides the axial velocity at 0.078*D* upstream of the propeller for the three propeller operating conditions considered. Linear interpolation was performed between the six sPIV measurement planes to obtain the axial velocity at the vertical and lateral positions traced by a blade section at a given radial coordinate. The results are presented as the ratio of the velocity data obtained for the pylon-on and pylon-off configurations. A radial coordinate of $r/R = 0.65$ is considered, because the blade pressure distribution was measured at this position. Markers are indicated at two-degree intervals for clarity; note that the actual resolution of the data was higher.

In Fig. 5, a net decrease in inflow velocity is shown in the pylon wake, with a magnitude of about 19–25% of the local velocity measured for the pylon-off configuration. The maximum deficit occurred in the center of the wake at a blade position of $\phi = 180°$, as expected. Both the wake width and maximum velocity deficit decreased with increasing propeller thrust. This is due to the favorable pressure gradient imposed by the propeller. Similar results have been presented in literature for turbulent wakes in favorable pressure gradients (e.g., [25]). Outside of the wake region, an additional change in velocity is observed due to the installation of the pylon. This is due to the deceleration of the flow field near the pylon trailing edge.

The velocity deficit in the pylon wake introduces a nonuniformity into the propeller inflow. To quantify the

Table 3 sPIV data acquisition and postprocessing characteristics

Parameter	Value
Laser	Quantel Evergreen Nd:YAG 200 mJ
Cameras	PCO SensiCam (1280 pixel × 1024 pixel)
Objective	Zeiss 200 mm *f*/2.0 + 2× teleconverter
Field of view (FoV) size	152 mm × 212 mm
Vertical positions FoV ($-Z/R$)	0.34, 0.49, 0.69, 0.79, 0.89, 0.99
Number of image pairs	330
Acquisition frequency	3 Hz
Magnification	0.040
Digital resolution	6.0 pixel/mm
Pulse separation	15 μs
Free-stream particle displacement	5–7 pixel
Final interrogation window size	24 pixel × 24 pixel
Window overlap factor	50%
Vector spacing	2.0 mm
Velocity uncertainty ϵ_U/U_∞	0.036

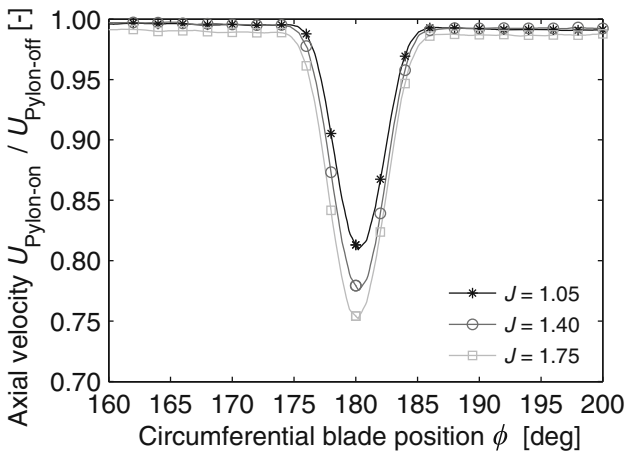

Fig. 5 Effect of propeller thrust setting on the wake velocity deficit experienced by a blade section at r/R = 0.65, 0.078D upstream of the propeller, $\beta = 0°$

resulting impact on the propeller response, the unsteady blade loads were analyzed at a radial station of $r/R \approx 0.65$. The surface-pressure transducers provided measurements on opposite sides of the blade at seven chordwise positions. The local pressure jump was computed by subtracting the pressure coefficients measured on the pressure and suction sides of the blades. Integration was then performed in the chordwise direction using the trapezoidal rule to obtain the local normal-force coefficient as a function of the circumferential blade position. In this process, the pressure jump measured at the pressure transducer closest to the blade leading edge ($x/c_b = 0.05$) was extended up to the leading edge, while at the trailing edge a pressure difference of zero was prescribed. Comparison with data obtained from CFD simulations of the isolated propeller, not discussed in this paper, showed that the associated integration error was less than 1%. Figure 6 presents the resulting development of the normal-force coefficient throughout the rotation, while Table 4 summarizes the corresponding numerical values. Estimates of the uncertainty of the data were computed from the scatter of repeated measurements taken for the pylon-off configuration and are indicated by the error bars plotted in the top left of the subplots of Fig. 6. Data markers are displayed at 15° intervals for clarity. The circumferential blade position is defined with respect to the leading edge of the blade at a radial station of $r/R \approx 0.65$.

Figure 6 shows a sinus-like variation of the sectional normal-force coefficient during the rotation for the pylon-off configuration. This is ascribed to a slight angular inflow to the measurement setup, caused by a flow perturbation due to the presence of the inflow measurement infrastructure. The corresponding inflow angle was estimated from the data to be approximately 0.2°. With the pylon installed, an impulsive increase in the blade loading occurred during the wake encounter. Analysis of the pressure distributions showed that the increase of the normal force was mainly due to a localized rise of the pressure jump across the leading-edge part of the blade, as illustrated in Fig. 7 for the intermediate thrust case ($J = 1.40$). The pressure distribution on the rear of the blades was hardly affected by the installation of the pylon.

The largest impact of the wake on the sectional blade normal force occurred at the low thrust setting ($J = 1.75$). In this operating regime, the normal force increased by approximately 35% during the wake encounter when compared to the steady-state value. Considering the root mean square of the normal-force fluctuations, a similar

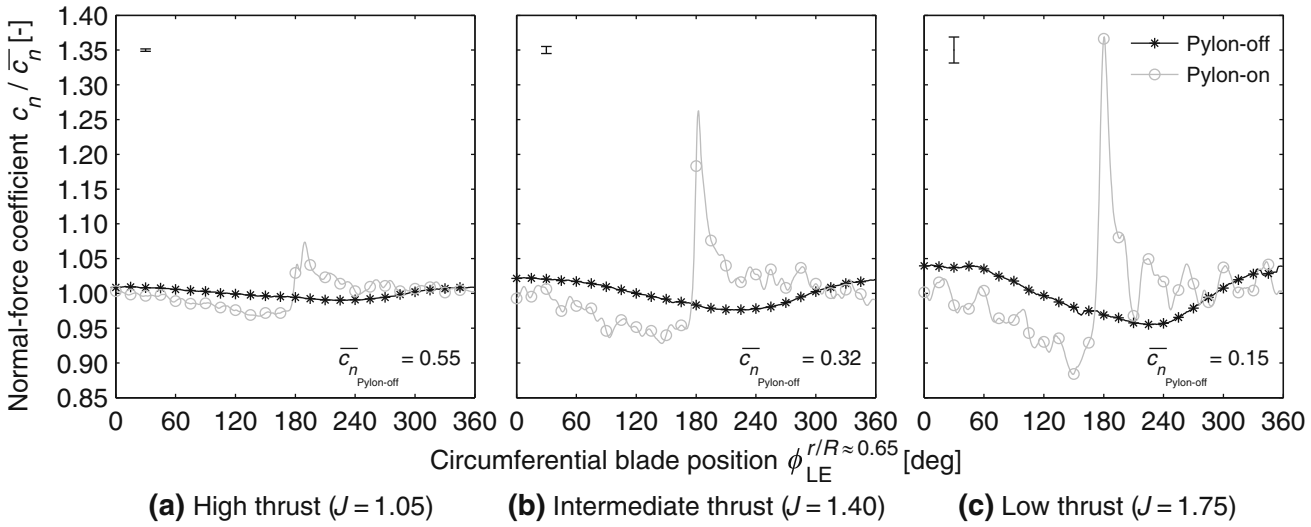

Fig. 6 Effect of pylon installation on the normalized sectional normal-force coefficient at $r/R \approx 0.65$, $\beta = 0°$. An error bar is displayed at the top left of each subplot

Table 4 Effect of pylon installation on the sectional blade-loading characteristics at $r/R \approx 0.65$, $\beta = 0°$

J	$\overline{c_n}$		$\frac{\overline{c_n}_{Pylon-on}}{\overline{c_n}_{Pylon-off}}$	$RMS\{c_n - \overline{c_n}\}/\overline{c_n}$		$\frac{c_{n\text{wake}}}{\overline{c_n}}$	$\phi_{c_{n\text{wake}}}$
	Pylon-off	Pylon-on		Pylon-off	Pylon-on		
1.05	0.546	0.549	1.004	0.006	0.020	1.074	190°
1.40	0.320	0.334	1.042	0.016	0.049	1.263	183°
1.75	0.150	0.168	1.120	0.030	0.070	1.369	181°

The normal-force coefficient at the maximum impact of the wake encounter is indicated by $c_{n\text{wake}}$

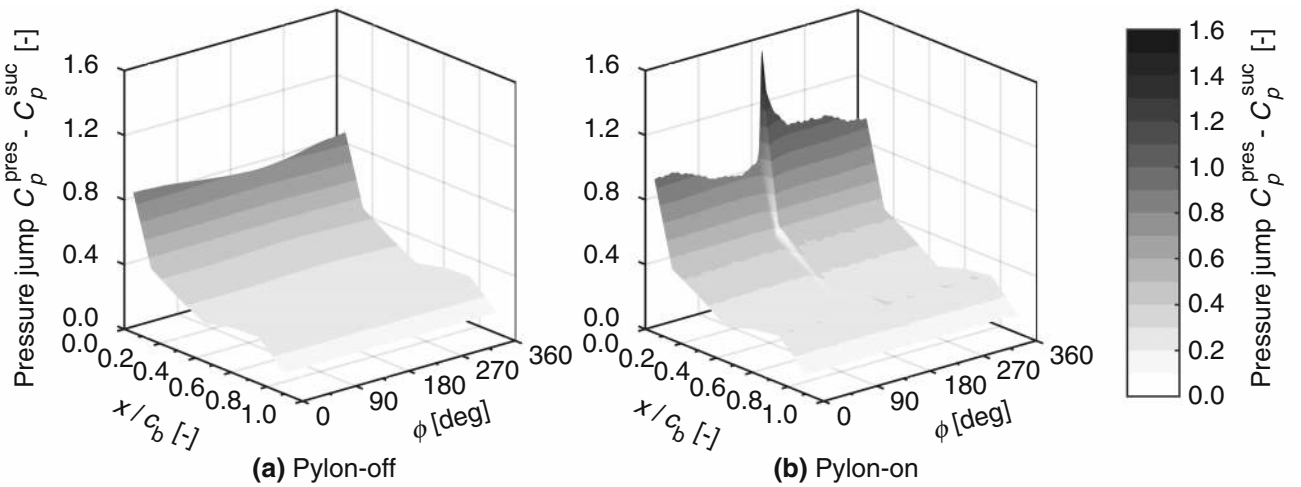

Fig. 7 Effect of pylon installation on the pressure jump throughout the rotation at $r/R \approx 0.65$, $J = 1.40$, $\beta = 0°$

conclusion can be drawn. Again, with increasing thrust setting, the relative amplitude of the oscillations of the normal force decreased. The reduction in impact of the wake impingement with increasing thrust setting has three reasons. First, for a given velocity deficit in the propeller inflow, the absolute change in angle of attack experienced by the blade section decreases with increasing rotational velocity, hence increasing the rotational speed of the propeller. This effect is further enhanced by the reduction in wake deficit with increasing thrust coefficient, as shown in Fig. 5. Second, with increasing thrust setting, the inflow-angle change due to the wake encounter loses importance relative to the steady value, since the steady-state angle of attack of the blade increases with decreasing advance ratio.

Finally, the reduced frequency of the wake-impingement perturbation increases with increasing rotational speed, and hence the thrust setting. With increasing reduced frequency, the amplitude of the unsteady load perturbation decreases [26]. For the given blade geometry and operating parameters, the reduced frequency k equaled 0.28, 0.26, and 0.24 at $r/R \approx 0.65$ at the fundamental frequency for the high, intermediate, and low thrust conditions, respectively. The unsteady response of the blades also leads to a phase lag between the peak normal-force response and the location of maximum velocity deficit in the wake ($\phi = 180°$). This phase lag increases with the thrust setting due to the associated increase in reduced frequency of the perturbation problem.

Outside of the pylon-wake region, the blade responses for the pylon-off and pylon-on configurations also differed. Ahead of the wake encounter, the blades experienced a slight change in loading due to the local deceleration of the flow field near the pylon trailing edge. After the wake encounter, the blade response slowly recovered toward the values recorded for the pylon-off configuration. The load oscillations occurring in this part of the rotation for the pylon-on configuration seem related to the excitation of the blades due to the wake passage. However, it is unknown whether they were the result of purely aerodynamic effects, or possibly a structural response of the blades.

The variations of the suction-peak pressure coefficient were analyzed in the frequency domain to assess the tonal and broadband components of the blade-load fluctuations resulting from the installation of the pylon. Repeated measurements provided 6–17 spectra for each operating condition. Ensemble averaging was performed to obtain the final results, as plotted in Fig. 8. Low-amplitude electronic noise was present in the pylon-off data at frequencies equal to integer multiples of 50 Hz, corresponding to mains interference.

The frequency spectra presented in Fig. 8 significantly differ between the three thrust settings. Comparing the pylon-off configurations, a strong increase of the broadband component of the pressure fluctuations can be observed at the high thrust setting (Fig. 8a). This was due to the increased turbulence levels induced by a leading-edge vortex, caused by the high blade sweep. The existence of this leading-edge vortex was confirmed by analysis of the data from the pressure sensors at the other locations on the blade and numerical simulations of the isolated propeller. For the lower thrust cases (Fig. 8b, c), the leading-edge vortex was less prominent ($J = 1.40$) or absent ($J = 1.75$). Therefore, the broadband response is lower for these thrust settings. Instead, at the intermediate and low thrust settings, the spectra were dominated by the fundamental tone at the shaft frequency, while the levels of the harmonics were comparatively low. The observed tonal components in the pylon-off data were due to the slight inflow angularity discussed in conjunction with Fig. 6, and should be considered as an artifact rather than an expected feature of the investigated configuration.

For the pylon-on configuration, the periodic impulsive increase in suction-peak pressure during the wake encounter led to an increase of the power levels at the shaft order, and especially its harmonics. The largest tonal pressure oscillations occurred at the intermediate thrust setting (Fig. 8b). The increased turbulence intensity in the pylon wake increased the broadband response of the blades at all thrust settings when compared to the pylon-off configuration.

The RSB data were evaluated to investigate the impact of the pylon installation on the integral propeller loads. Figure 9 depicts the integral time-averaged propeller

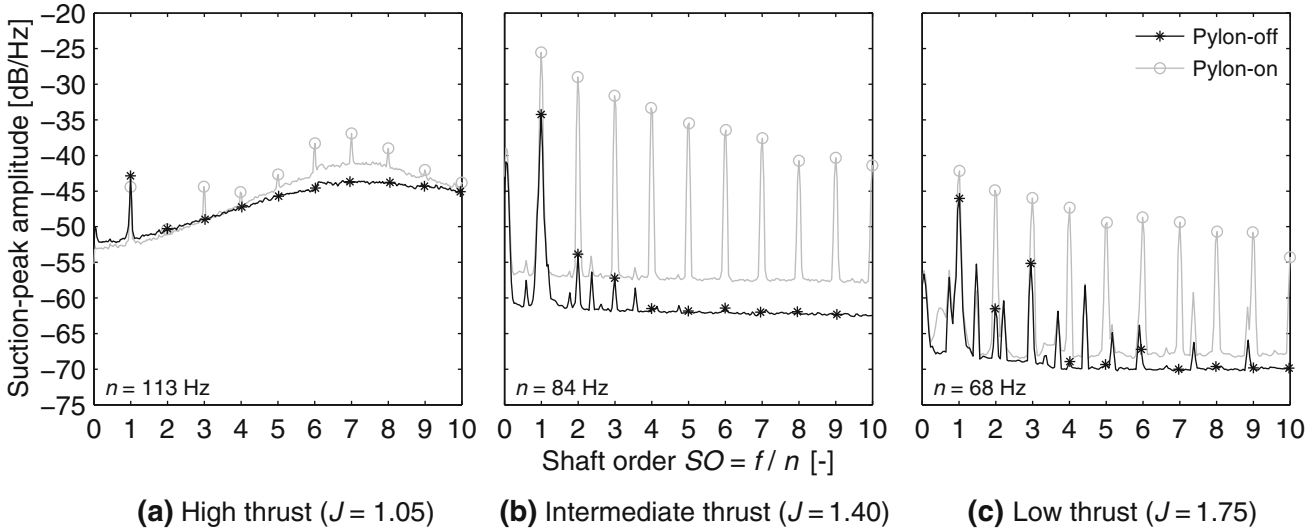

Fig. 8 Effect of pylon installation on the frequency spectra of the suction peak pressure coefficient at $r/R \approx 0.65$, $x/c_b = 0.05$, $\beta = 0°$

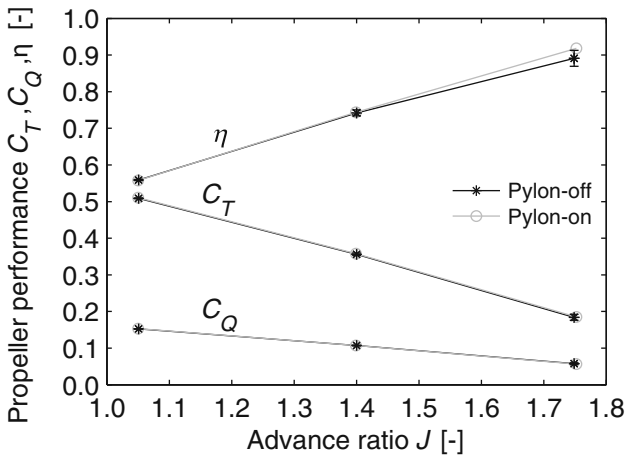

Fig. 9 Effect of pylon installation on the time-averaged propeller performance, $\beta = 0°$

Table 5 Effect of pylon installation on the time-averaged propeller thrust coefficient; $\beta = 0°$

J	C_T		ΔC_T (%)
	Pylon-off	Pylon-on	
1.05	0.509 ± 0.001	0.510 ± 0.001	+0.2
1.40	0.356 ± 0.004	0.357 ± 0.004	+0.3
1.75	0.183 ± 0.008	0.187 ± 0.008	+1.8

performance measured under symmetric inflow conditions, at the three thrust settings considered throughout the paper. The corresponding numerical values for the thrust coefficient are summarized in Table 5. The uncertainty of the data is indicated by error bars displayed at each data point for the pylon-off configuration. It was computed as the standard deviation of all available repeated measurements.

From Fig. 9 and Table 5, it is concluded that the impingement of the pylon wake did not significantly alter the time-averaged integral propeller performance. At all operating points, the measured changes in propeller thrust were within the variability of the RSB data. Similarly, small differences were measured for the torque coefficient. This agrees with the measurement data of Gentry et al. [15], who also concluded that the effect of the pylon wake on the steady-state propeller performance was negligible. The favorable interference effect due to the nacelle that was observed in that study could not be reproduced here, since no nacelle was present upstream of the propeller. Note that the RSB results differ from the higher changes in sectional normal-force coefficient derived from the pressure transducers installed in the propeller blades (Table 4). However, integrated over the blade, the overall increase in thrust could be smaller than predicted locally at $r/R \approx 0.65$ due to variations of the unsteady response of the blades along the span.

3.1.2 Asymmetric inflow conditions

The introduction of angular inflow to the pylon-on configuration leads to nonzero loading on the pylon. To assess whether this induced a strong modification of the pylon wake, Fig. 10 provides a comparison of the propeller inflow experienced under symmetric and asymmetric inflow conditions. The low thrust case is considered, while the measurements in angular inflow were performed at a sideslip angle of $\beta = -6°$. For clarity, markers are again displayed at two-degree intervals.

Figure 10 shows that for the case with angular inflow, the location of the maximum velocity deficit was shifted to a lower circumferential angle than for the symmetric configuration. Also, the flow deceleration outside of the pylon wake increased due to the operation at sideslip. Both effects are due to the increased loading on the pylon, which intensified the impact of the pylon on the surrounding flow field. Yet, the relative velocity deficit and wake width were comparable for both cases. Therefore, the impact of the wake encounter on the propeller blade loads is expected to be similar for the symmetric and asymmetric inflow configurations. To test this hypothesis, Fig. 11 provides the phase-averaged sectional loading data for the pylon-off and pylon-on configurations, with and without angular inflow. The low thrust condition ($J = 1.75$) is considered, while markers are again plotted at 15° intervals. The associated numerical data are provided in Table 6.

Figure 11 confirms that the operation of the isolated propeller under angular-inflow conditions introduced unsteady loading on the blades. The cyclic changes in the effective velocity experienced by the blade sections resulted in angle-of-attack perturbations during the rotation, leading to the expected sinusoidal load variations [27, 28]. With the pylon present, a significant shift is observed in the sectional blade loading when comparing

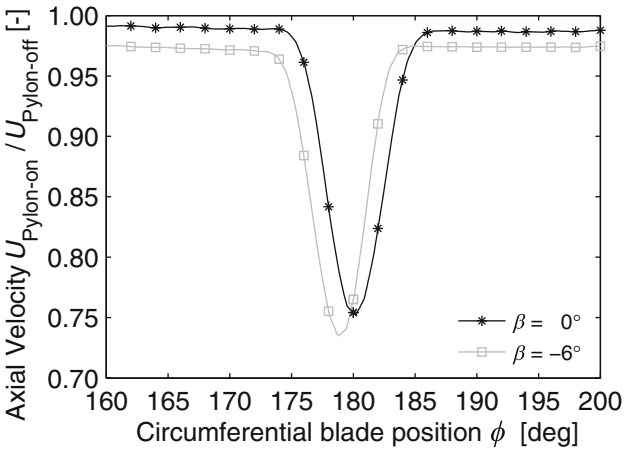

Fig. 10 Effect of angular inflow on the wake velocity deficit experienced by a blade section at $r/R = 0.65$, $0.078D$ upstream of the propeller, $J = 1.75$

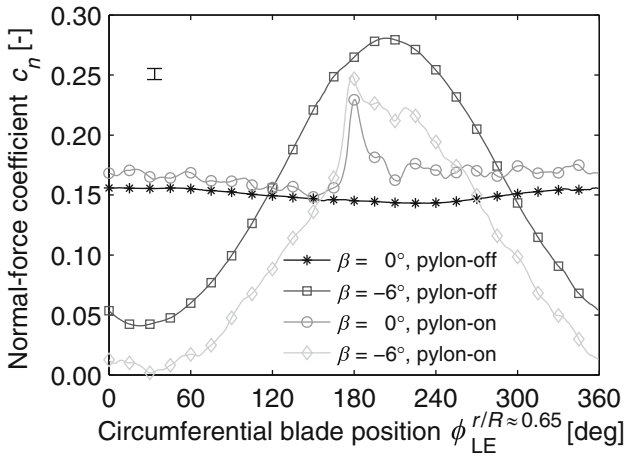

Fig. 11 Effect of pylon installation and angular inflow on the sectional normal-force coefficient at $r/R \approx 0.65$, $J = 1.75$. Error bar is displayed at the top left

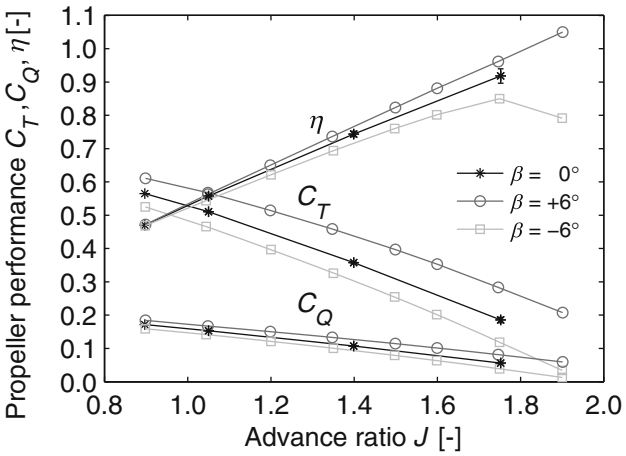

Fig. 12 Effect of angular inflow on the time-averaged propeller performance, pylon-on

Table 6 Effect of pylon installation and angular inflow on the sectional blade-loading characteristics at $r/R \approx 0.65$, $J = 1.75$

Configuration	$\overline{c_n}$		$\frac{\overline{c_n}^{\beta=-6°}}{\overline{c_n}^{\beta=0°}}$	RMS$\{c_n - \overline{c_n}\}/\overline{c_n}$	
	$\beta = 0°$	$\beta = -6°$		$\beta = 0°$	$\beta = -6°$
Pylon-off	0.150	0.156	1.039	0.030	0.538
Pylon-on	0.168	0.103	0.614	0.070	0.749

the cases at zero and negative sideslip. Since the blade normal force was affected throughout the entire rotation, this cannot be due to the more localized pylon-wake encounter. Instead, the offset is ascribed to an interaction with the tip vortex of the pylon. Depending on its direction of rotation relative to the propeller, the tip vortex either increased or decreased the rotational velocity experienced by the blade sections. Consequently, the effective advance ratio was modified due to the interaction with the tip vortex, thereby affecting the propeller blade loads.

Apart from the offset due to the tip-vortex interaction, the sinusoidal normal-force oscillations due to the sideslip angle were similar for the pylon-off and pylon-on configurations. Therefore, it is concluded that the pylon did not appreciably modify the effective incidence angle experienced by the propeller. This opposes the conclusions drawn by Magliozzi [8], who attributed a drop in measured noise levels for the pylon-on configuration at angle of attack to a flow-straightening effect due to the pylon.

Figure 11 also shows that the wake-impingement effects were comparable under symmetric and asymmetric inflow conditions, apart from a 4-degree phase offset between the blade positions corresponding to the peak normal-force perturbation. This was due to the asymmetry of the wake profile at sideslip, which resulted in a shift of the maximum velocity deficit toward the blades entering the wake region (Fig. 10), hence reducing the circumferential blade position of maximum wake impact.

The shift in blade normal force due to the interaction with the pylon tip vortex strongly modified the integral propeller performance. Figure 12 presents the performance diagrams measured for the pylon-on configuration, at sideslip angles of 0° and ±6°. The corresponding numerical data are provided in Table 7. Linear interpolation was applied to report the thrust-coefficient values at the three advance ratios considered in the rest of the paper. The change in effective advance ratio due to the interaction with the pylon tip vortex is represented by the parameter ΔJ_β. The value of this parameter was approximated by comparing the advance ratios required to obtain the same thrust-coefficient value under symmetric and asymmetric inflow conditions.

The performance curves plotted in Fig. 12 show a critical change of the system's sensitivity to the pylon-installation effects due to the angular inflow, confirming the trends observed in the sectional loading data (Fig. 11) and those discussed before by Patterson and Bartlett [16]. Operation at positive sideslip significantly increased the propeller thrust and torque at constant advance ratio. For this configuration, the effective advance ratio sensed by the blades was decreased by 0.13–0.17 when compared to the symmetric case. Considering the definition of the sideslip angle (Fig. 3a), this implies that the effective advance ratio experienced by a pylon-mounted pusher propeller decreases due to the tip-vortex interaction if the propeller rotation direction is inboard-up. In this way, a given thrust coefficient can be obtained at reduced rotational speed of the propeller, which is beneficial from both aerodynamic and acoustic points of view. It should be noted that the measured effects due to the pylon tip vortex might have been amplified due to the absence of a nacelle at the tip of the pylon in the test setup.

Table 7 Effect of angular inflow on the time-averaged propeller thrust coefficient, pylon-on

J	C_T			ΔJ_β	
	$\beta = 0°$	$\beta = +6°$	$\beta = -6°$	$\beta = +6°$	$\beta = -6°$
1.05	0.510	0.567	0.464	−0.13	+0.10
1.40	0.357	0.438	0.302	−0.16	+0.10
1.75	0.187	0.281	0.119	−0.17	+0.11

3.2 Aeroacoustic interaction effects

The unsteady blade loads resulting from the pylon-wake encounter introduce an additional noise-generating mechanism compared to the pylon-off configuration. The periodic impingement phenomenon causes additional tonal noise emissions. The interaction of the blades with the increased turbulence intensity in the pylon wake constitutes a secondary effect, which might affect the broadband noise emissions.

3.2.1 Symmetric inflow conditions

Sound spectra were computed from the inflow microphone data to compare the propeller noise emissions with and without the pylon. Figure 13 presents the spectra acquired at the high, intermediate, and low thrust settings. The data were obtained using the microphone corresponding to an axial emission angle in the propeller plane ($\theta_e = 90°$) and a circumferential position perpendicular to the pylon ($\phi = 90°$). For reference, measurements of the background noise were taken using a dummy spinner. The corresponding levels are indicated in Fig. 13 by the lines without markers. Note that wind-tunnel fan noise overpowered the propeller noise at frequencies below approximately 400 Hz.

The spectra depicted in Fig. 13 display typical propeller noise signatures. For the pylon-off configuration, the noise emissions were dominated by the fundamental propeller tone (1BPF). With the pylon present, on the other hand, the noise levels increased and the harmonics contributed to the overall tonal noise level at all operating conditions considered. This is due to the impulsive blade-loading change during the pylon-wake encounter (Fig. 6), and was also observed before by other researchers [10]. The overall noise penalty was smallest in high thrust conditions ($J = 1.05$, Fig. 13a), because at this setting the thickness and steady-loading noise sources associated with the isolated propeller were dominant. At the selected microphone position, the level of the fundamental tone even decreased by 2 dB due to the pylon installation. At this frequency, the wavelength of the acoustic signal was of the order of the propeller diameter. Therefore, the reduction of the tonal noise level due to the pylon installation could have been due to local destructive interference between the various noise sources. This is treated in more detail in the discussion of Fig. 15. At the other two operating conditions ($J = 1.40$ and $J = 1.75$, Fig. 13b, c), the thickness and steady-loading sources were weaker; hence, the noise penalty due to the pylon installation was larger. This trend of increasing installation impact with decreasing thrust condition agrees with the observations published before by Block [6, 14].

The installation of the pylon did not significantly affect the measured broadband noise emissions. These only stood out of the background noise for the high and intermediate thrust cases (for $f > 250$ Hz and $f > 2500$ Hz, respectively). At both thrust settings, the levels of the broadband noise emissions were the same for the pylon-off and pylon-on configurations. Apparently, the increase in the random fluctuations of the suction-peak pressure caused by the installation of the pylon (Fig. 8) was insufficient to modify the broadband component of the noise. The strong increase in broadband noise emissions at the highest thrust setting observed for the isolated propeller is as expected, considering the spectra of the suction-peak pressure discussed before.

For the pylon-on configurations, the spectra contained an additional tone when compared to the pylon-off cases at a frequency of around 1770 Hz. The propeller thrust setting did not affect the frequency and amplitude of this tone, which was attributed to vortex shedding from the pylon trailing edge. This was concluded from analysis of the velocity fields downstream of the pylon acquired with the sPIV setup, as shown in Fig. 14. A clear vortex street can be seen traveling downstream, with four shedding periods visible in the field of view. The shedding length was approximated at 26 mm, while the local axial velocity equaled around 45 m/s, leading to a shedding frequency of about 1730 Hz. This is within 2% of the frequency of the tone observed in the sound spectra (Fig. 13), hence confirming that the tone was indeed caused by vortex shedding.

Considering the negligible impact of the pylon installation on the broadband noise emissions, the remainder of this subsection focuses on the tonal noise levels. Figure 15 compares the pressure waveforms corresponding to the sum of the first ten propeller tones for the pylon-off and pylon-on configurations.

Figure 15 shows that for the pylon-off configuration, the shapes of the pressure waveforms were similar among different thrust settings. A six-per-revolution cycle can be seen, corresponding to the individual blade passages. The installation of the pylon increased the complexity of the acoustic pressure signals, causing a modification of the noise emissions as discussed before under Fig. 13. The

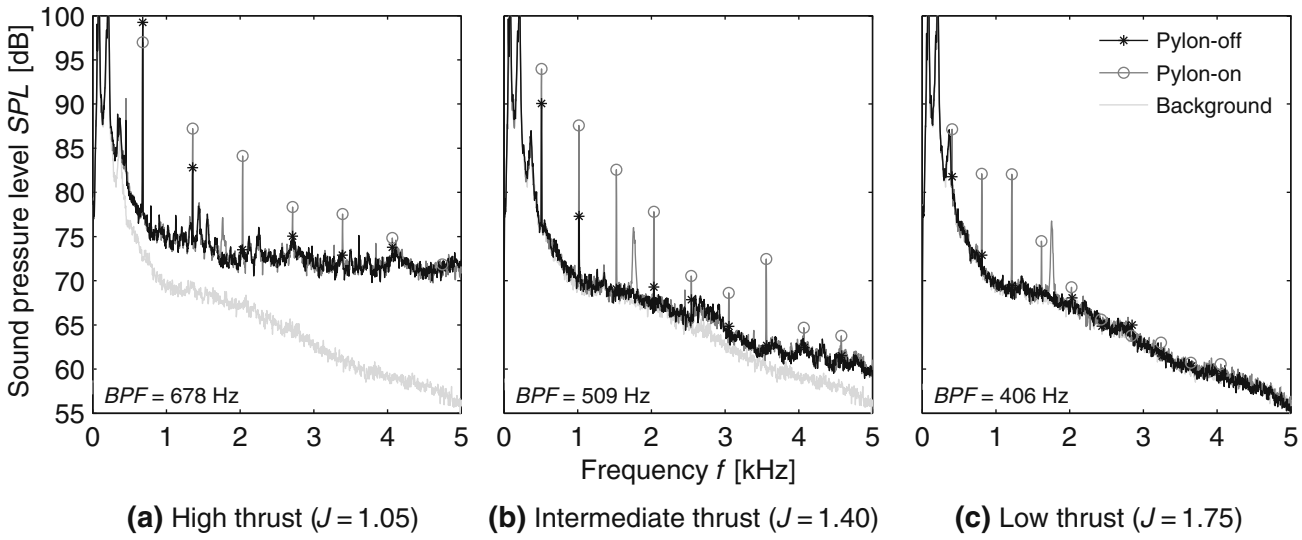

Fig. 13 Effect of pylon installation on the propeller noise spectra, $\theta_e = 90°$, $\phi = 90°$, $\beta = 0°$

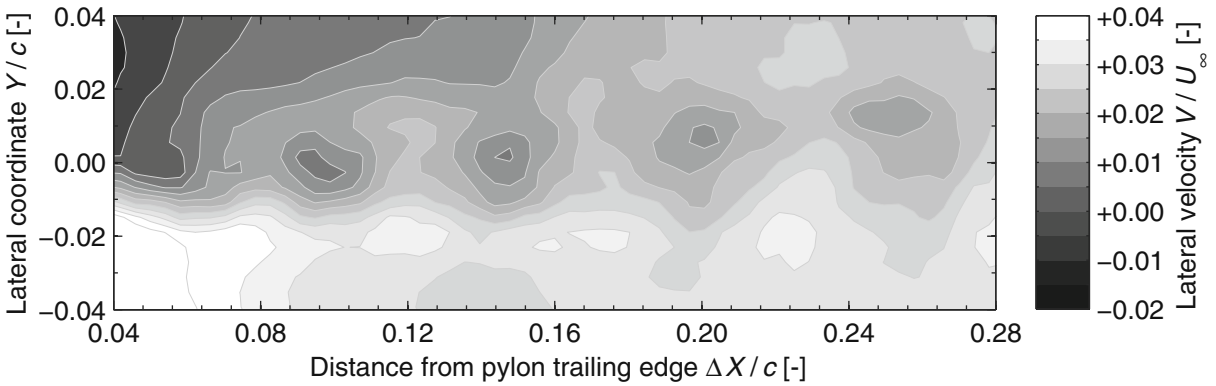

Fig. 14 Contours of the lateral velocity downstream of the pylon trailing edge indicating vortex shedding, $J = 1.40$, $\beta = 0°$

intermediate and low thrust cases displayed a comparable behavior. The amplitude of the positive pressure peaks increased due to the installation of the pylon, and the impulsive pressure changes on the blades occurring during the wake encounter enriched the harmonic content of the acoustic signals. At the high thrust setting, a different pattern is observed. The interaction noise component effectively canceled part of the thickness and steady-loading noise generated by the isolated propeller. As a result, at this thrust setting, the overall sound pressure level of the propeller tones decreased due to the installation of the pylon at the considered observer position.

Besides the pronounced impact on the levels, the installation of the pylon also affected the directivity of the propeller noise emissions. In the circumferential direction, the noise penalty due to the pylon installation was relatively constant for the range of angles covered by the inflow microphones. Therefore, only the results measured using the microphone positioned perpendicular to the pylon ($\phi = 90°$) are discussed here. Figure 16 presents the corresponding total tonal noise levels as a function of the axial emission angle. An interaction noise metric (labeled 'Interaction') was defined as the sound pressure level corresponding to the difference between the pressure signals for the pylon-on and pylon-off configurations. The resulting values are indicative of the relative importance of the noise source associated with the pylon-wake effect and the noise levels emitted by the isolated propeller.

The data displayed in Fig. 16 present a clear directivity effect. The additional noise due to the installation of the pylon was especially pronounced in the upstream direction. Regardless of the propeller thrust setting, the interaction noise peaked at an axial emission angle of about 50°. The largest installation impact occurred at the low thrust setting, with noise penalties of up to 24 dB. Consequently, the installation of the pylon strongly reduced the sensitivity of

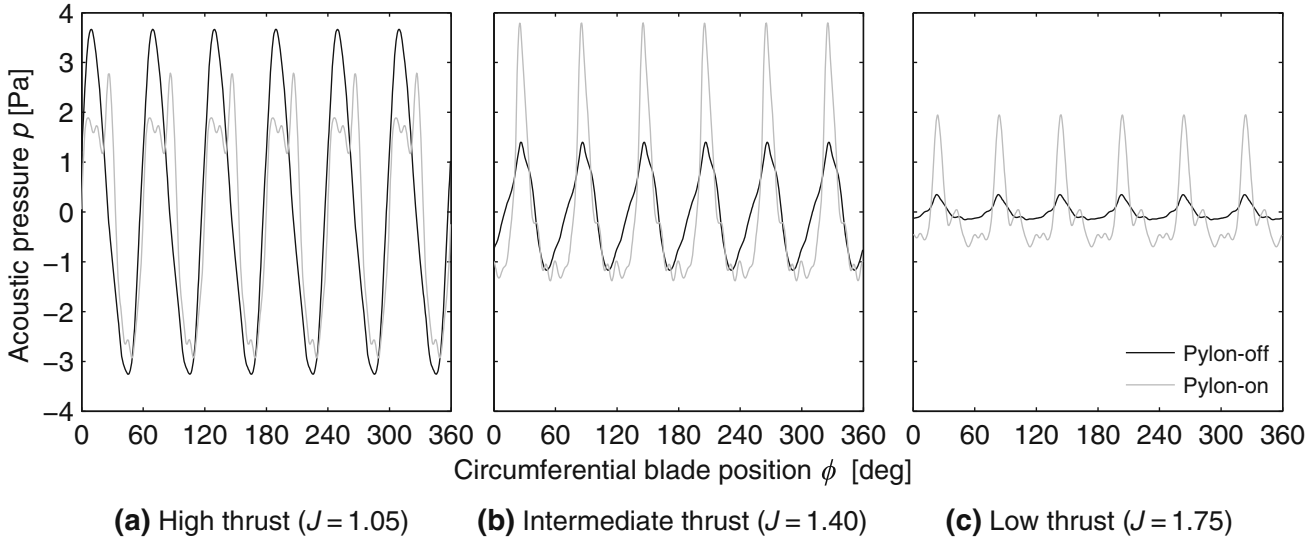

Fig. 15 Effect of pylon installation on the acoustic-pressure waveforms corresponding to the sum of the first ten propeller tones, $\theta_e = 90°$, $\phi = 90°$, $\beta = 0°$

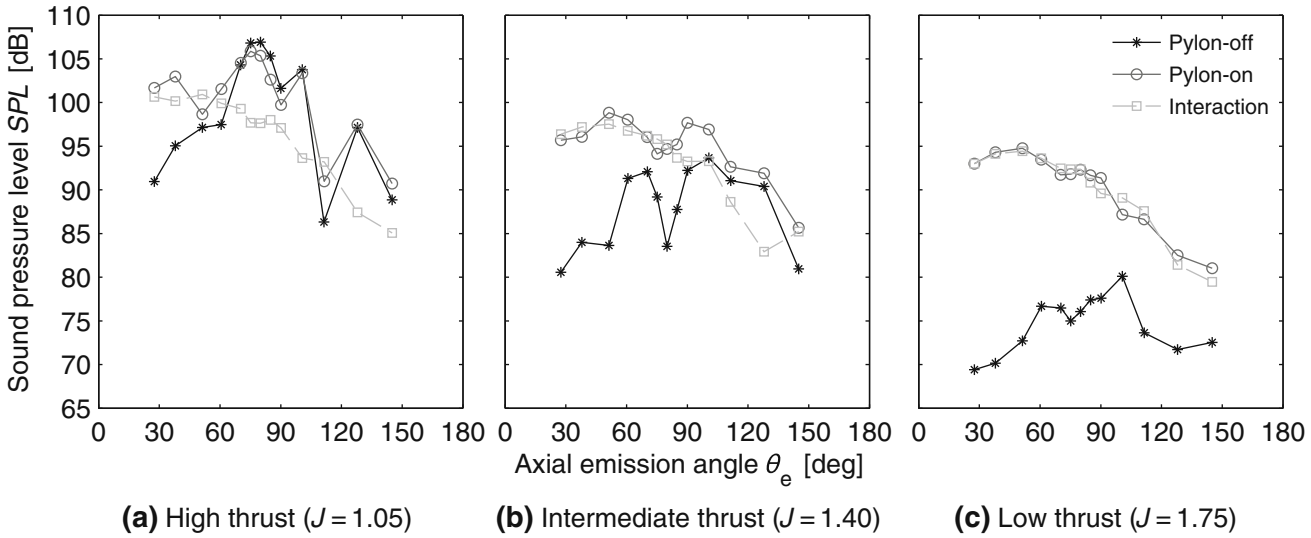

Fig. 16 Effect of pylon installation on the axial directivity of the propeller's tonal noise emissions, $\phi = 90°$, $\beta = 0°$

the noise emissions to the propeller thrust setting. For the isolated propeller, a difference of 10–20 dB was present between the high and low thrust cases. With the pylon installed, this decreased to 5–10 dB. The measured directivity of the interaction noise due to the installation of the pylon matches with numerical results computed by Stürmer and Yin [18] for the front row of a contra-rotating open rotor with high blade sweep. Block [6, 14], on the other hand, measured a strong noise penalty in both the forward direction and the aft direction. The exact reason for this difference is unknown, but it could be related to the significantly different blade shape used in the current experiment compared to the model used by Block.

The directivity patterns measured for the isolated propeller showed unexpected local drops in the noise level at all three advance ratios. Analysis of the pressure waveforms showed that this was due to interference between the various noise sources, which might have locally reduced the measured sound pressure level. For the fundamental tone, with wavelength of the order of the propeller diameter, the pressure signals at $\theta_e = 80°$ and $\theta_e = 90°$ were completely out of phase. No significant additional peaks were observed in the spectra apart from those corresponding to the individual blade passages. Therefore, the possibility of reflections influencing the data seems to be excluded.

3.2.2 Asymmetric inflow conditions

Operation of the propeller at angle of attack affects the propeller noise emissions in two different ways [29]. First, the oscillatory blade loading (Fig. 11) introduces a source of unsteady-loading noise. Second, the crossflow modifies the local Mach number of the blade sections when rotating toward the observer. The recorded noise levels are increased if the blades travel toward the microphones with increased Mach number, and vice versa. The relative impact of the two effects depends on the propeller operating condition. This is clearly illustrated in Fig. 17, which presents the axial directivity patterns measured at the high and low thrust settings (Fig. 17a, b). For the latter, also the data acquired for the pylon-on configuration are included (Fig. 17c). Results are presented for sideslip angles of 0°, +6°, and −6°, except for the high thrust case for which only data were available at the negative angle.

The directivity patterns shown in Fig. 17a, b highlight the shift in the acoustic impact of the sideslip angle with the propeller operating point. For the circumferential directivity angle considered here ($\phi = 90°$), the blades traveled toward the microphones with increased Mach numbers for the positive sideslip case. Therefore, at that condition the highest noise penalty was observed at all thrust settings, since both the unsteady blade loads and convective-amplification effects resulted in increased noise levels. For the low thrust case at positive sideslip, the resulting noise penalty was up to 12 dB when compared to the symmetric-flow case. At $\beta = -6°$, on the other hand, the unsteady blade loads increased the noise levels, which was opposed by a noise reduction due to the reduced blade velocity in the direction of the microphones. Figure 17 shows that the effects due to the unsteady blade loads were dominant at the low thrust setting, while for the high thrust case the blade Mach number effects had the largest impact on the overall noise levels. This was confirmed by analysis of the pressure waveforms corresponding to the data depicted in Fig. 17.

As shown in Fig. 17c, the installation of the pylon also increased the noise emissions under angular-inflow conditions. However, the noise levels were lower than those for the symmetric case in most of the directivity range. Especially for the case at positive sideslip, the noise penalty due to the pylon installation was significantly smaller than for the symmetric configuration. To investigate the angular-inflow effects in more detail, Fig. 18 presents the waveforms of the acoustic pressure for the three sideslip cases at the low thrust condition ($J = 1.75$). Note that the results were obtained at constant advance ratio, which implies that the propeller loading differed considerably between the three cases (Fig. 12).

The pressure traces plotted in Fig. 18 confirm the complex changes to the soundfield due to the operation at sideslip discussed before. At the negative sideslip angle (Fig. 18b), the shape of the waveform corresponding to the isolated propeller (pylon-off) was modified due to the addition of the noise source caused by the unsteady blade loads. Operation at positive sideslip (Fig. 18c) increased the amplitude of the isolated-propeller noise, due to both the unsteady blade loads and the blade Mach number effect.

The interaction effects due to the pylon installation were strongly affected at positive sideslip. In this inflow regime, the amplitudes of the positive pressure peaks were hardly changed by the installation of the pylon, as opposed to the results for the symmetric case and at negative sideslip. Instead, the pylon-wake impingement led to strong

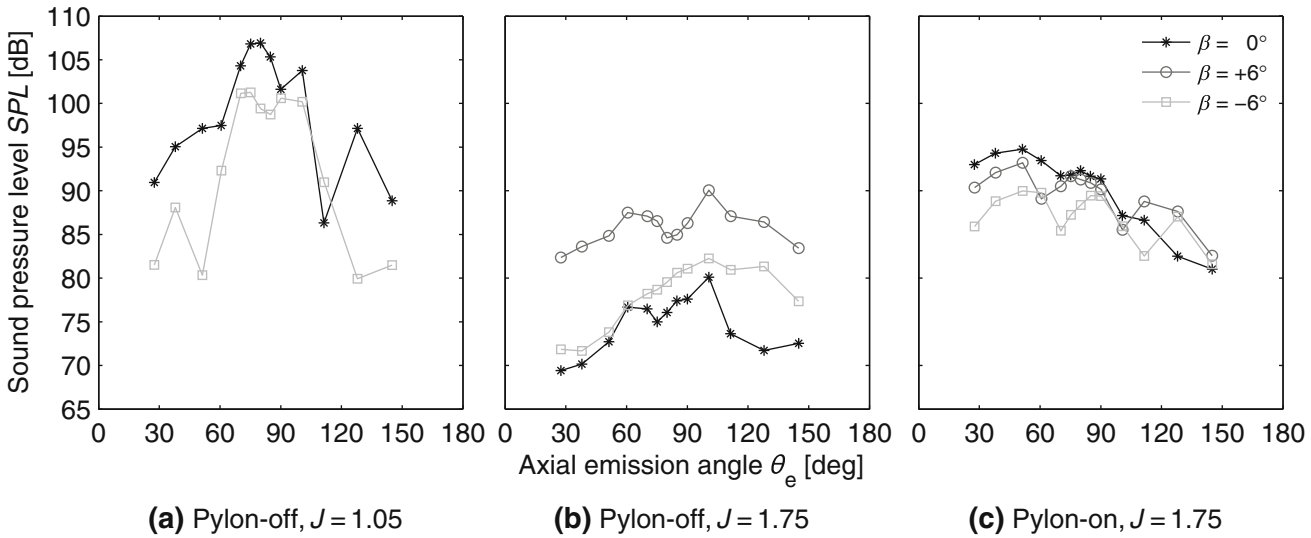

Fig. 17 Effect of angular inflow on the axial directivity of the propeller's tonal noise emissions, $\phi = 90°$

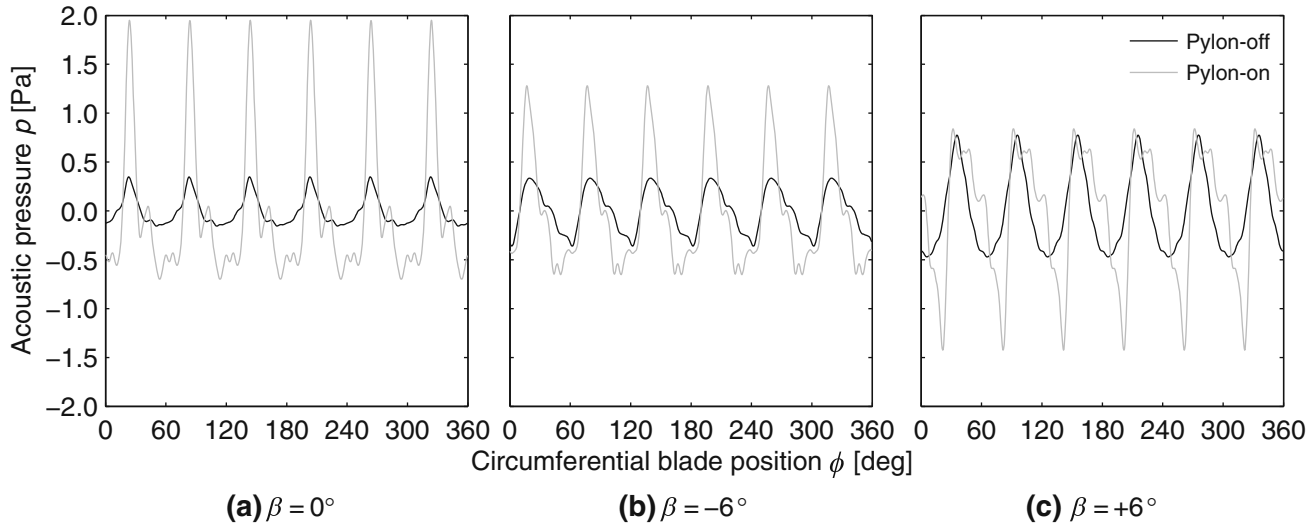

Fig. 18 Effect of pylon installation and angular inflow on the acoustic-pressure waveforms corresponding to the sum of the first ten propeller tones, $J = 1.75$, $\theta_e = 90°$, $\phi = 90°$

negative peaks in the acoustic waveform. This is likely related to the concurrent effects of the angle-of-attack perturbations due to the operation at sideslip and the installation of the pylon. At $\beta = +6°$, the wake encounter occurred in the part of the rotation where the blade angle of attack decreased due to the angular inflow. Therefore, the velocity deficit in the pylon wake locally *reduced* the angle-of-attack disturbance experienced by the propeller blades. Consequently, the wake impingement resulted in an additional change of sign of the blade-loading gradient when compared to the cases at $\beta = 0°$ and $\beta = -6°$. This explains the additional negative peak in the acoustic waveforms and stresses the importance of proper consideration of the propeller rotation direction for optimal integration of the propellers with the airframe.

4 Conclusions

This paper has presented a comprehensive analysis of the aerodynamic and aeroacoustic interaction effects occurring for pylon-mounted pusher propellers. The unique evaluation of the flow fields between the pylon and the propeller showed that the suction of the propeller reduces the severity of the pylon-wake encounter. The wake width and velocity deficit decrease with increasing thrust setting due to the favorable pressure gradient imposed by the propeller.

Measurements of the integral propeller performance confirmed previously published results by showing that the passage of the blades through the pylon wake has a negligible effect on the steady-state propeller thrust and torque. In contrast, the impact on the unsteady blade loads is significant, with a rapid increase in normal force during the wake encounter. The fluctuating blade pressures modify the amplitude, spectral content, and directivity of the propeller noise emissions, confirming results published in literature. The sensitivity of the interaction noise to the propeller operating point is lower than for the noise sources associated with the isolated propeller. Therefore, the installation of the pylon reduces the sensitivity of the propeller noise emissions to the thrust setting. The additional noise due to the unsteady blade loads peaks in the upstream direction, independent of the propeller thrust setting. At the lowest thrust setting considered, a maximum tonal noise penalty of 24 dB was measured. The impulsive nature of the pylon-wake encounter enriches the spectral content of the noise emissions. As such, the harmonics significantly contribute to the overall noise levels for the pylon-on configuration. Only the tonal noise levels were affected by the pylon-installation effects, while the broadband levels remained unchanged.

When operating in asymmetric inflow, the pylon tip vortex interacts with the propeller to result in significant modifications of the mean propeller performance. The rotational velocity components induced by the tip vortex affect the effective advance ratio sensed by the propeller, thereby changing the propeller rotational speed required to achieve a given thrust. The propeller performance is enhanced when the direction of rotation of the pylon tip vortex is opposite to that of the propeller. The noise penalty due to the pylon-installation effect can significantly decrease in this condition if the wake impingement occurs in the part of the rotation where the effective rotational velocity is reduced by the angular inflow. These novel results emphasize the importance of consideration of the propeller rotation direction for the optimal integration of the propellers with the airframe.

Acknowledgments The results presented in this paper were obtained by the APIAN-INF research partners in the framework of the transnational access program organized by the ESWIRP consortium, as part of the ESWIRP project (European Strategic Wind tunnels Improved Research Potential). The research leading to these results has received funding from the European Union Seventh Framework Programme (FP7-INFRASTRUCTURE-2008-1) under Grant agreement no. 227816. The authors would like to thank Hermann Holthusen for his efforts before and during the test campaign, and for providing assistance during the processing of the experimental data set. Moreover, the contributions of Kyle P. Lynch to the preparation, processing, and analysis of the PIV measurements are much appreciated. Mirjam Snellen is acknowledged for her involvement in the acoustic calibration part of the test program. Finally, thanks go to Eddy van den Bos for his crucial efforts in the definition of the structural design of the pylon model.

References

1. Guynn, M. D., Berton, J. J., Haller, W. J., Hendricks, E. S., Tong, M. T.: Performance and environmental assessment of an advanced aircraft with open rotor propulsion. NASA Langley Research Center, NASA-TM-2012-217772 (2012)
2. Mann, S., Stuart, C.: Advanced propulsion through the 1990s—An airframer's view. AIAA/SAE/ASME/ASEE 21st Joint Propulsion Conference, Monterey, CA, USA (1985). doi:10.2514/6.1985-1192
3. Page, M. A., Ivey, D. M., Welge, H. R.: Ultra high bypass engine applications to commercial and military aircraft. SAE Technical Paper 861720 (1986). doi:10.4271/861720
4. Farokhi, S.: Pressure-time history of pylon wake on a pusher propeller in flight. J. Propul. Power **6**(6), 758–768 (1990). doi:10.2514/3.23282
5. Magliozzi, B., Hanson, D. B., Amiet, R. K.: Propeller and propfan noise. In: Hubbard, H.H. (eds.) Aeroacoustics of flight vehicles: theory and practice—volume 1: noise sources, pp. 1–64, NASA Langley Research Center (1991)
6. Block, P. J. W., Gentry, G. L. Jr.: Directivity and trends of noise generated by a propeller in a wake. NASA Langley Research Center, NASA-TP-2609 (1986)
7. Woodward, R. P., Hughes, C. E.: Noise of a model counterrotation propeller with simulated fuselage and support pylon at takeoff/approach conditions. NASA Lewis Research Center, NASA-TM-101996 (1989)
8. Magliozzi, B.: Noise characteristics of a model counterrotating prop-fan. AIAA 11th Aeroacoustics Conference, Sunnyvale, CA, USA (1990). doi:10.2514/6.1987-2656
9. Shivashankara, B., Johnson, D., Cuthbertson, R.: Installation effects on counter rotating propeller noise. AIAA 13th Aeroacoustics Conference, Tallahassee, FL, USA (1990). doi:10.2514/6.1990-4023
10. Ricouard, J., Julliard, E., Omaïs, M., Regnier, V., Parry, A. B., Baralon, S.: Installation effects on contra-rotating open rotor noise. AIAA/CEAS 16th Aeroacoustics Conference, Stockholm, Sweden (2010). doi:10.2514/6.2010-3795
11. Elliott, D. M.: Initial investigation of the acoustics of a counter-rotating open rotor model with historical baseline blades in a low-speed wind tunnel. NASA Glenn Research Center, NASA-TM-2012-217258 (2012)
12. Czech, M. J., Thomas, R. H.: Open rotor aeroacoustic installation effects for conventional and unconventional airframes. AIAA/CEAS 19th Aeroacoustics Conference, Berlin, Germany (2013). doi:10.2514/6.2013-2185
13. Paquet, C., Julliard, E., Genoulaz, N., Ricouard, J., Spiegel, P.: Z08: low-speed aero-acoustic experimental characterization of open rotor installation on aircraft. AIAA/CEAS 20th Aeroacoustics Conference, Atlanta, GA, USA (2014). doi:10.2514/6.2014-2747
14. Block, P. J. W.: Experimental study of the effects of installation on single- and counter-rotation propeller noise. NASA Langley Research Center, NASA-TP-2541 (1986)
15. Gentry, G. L. Jr., Booth, E. R. Jr.: Effect of pylon wake with and without pylon blowing on propeller thrust. NASA Langley Research Center, NASA-TM-4162 (1990)
16. Patterson, J. C. Jr., Bartlett, G. R.: Effect of a wing-tip mounted pusher turboprop on the aerodynamic characteristics of a semi-span wing. AIAA/SAE/ASME/ASEE 21st Joint Propulsion Conference, Monterey, CA, USA (1985). doi:10.2514/6.1985-1286
17. Farokhi, S., Taghavi, R., Wetzel, K. K.: Frequency-domain analysis of fluctuating pressure on a pusher propeller blade surface. J. Aircr. **31**(1), 42–48 (1994). doi:10.2514/3.46453
18. Stürmer, A., Yin, J.: Installation impact on pusher CROR engine low speed performance and noise emission characteristics. Int. J. Eng. Syst. Modeling Simul. **4**(1–2), 59–68 (2012). doi:10.1504/IJESMS.2012.044844
19. Mauk, C. S., Farokhi, S.: The effect of unsteady blade loading on the aeroacoustics of a pusher propeller. AIAA/SAE/ASME/ASEE 29th Joint Propulsion Conference, Monterey, CA, USA (1993). doi:10.2514/6.1993-1805
20. Crozier, P.: APIAN installed tests in the ONERA S1MA wind tunnel. AIAA 39th Aerospace Sciences Meeting and Exhibit, Reno, NV, USA (2001). doi:10.2514/6.2001-580
21. Frota, J., Maury, E.: Analysis of APIAN high speed isolated test results—acoustics and aerodynamics. Air Space Europe **3**(3–4), 87–92 (2001). doi:10.1016/S1290-0958(01)90064-4
22. Philipsen, I., Hoeijmakers, H., Hegen, S.: An overview of advanced propeller simulation tests in the German Dutch Wind Tunnels. AIAA 22nd Aerodynamic Measurement Technology and Ground Testing Conference, St. Louis, MO, USA (2002). doi:10.2514/6.2002-2920
23. Sinnige, T., Ragni, D., Eitelberg, G., Veldhuis, L. L. M.: Mitigation of pusher-propeller installation effects by pylon trailing-edge blowing. J. Aircr. **54**(1), 292–300 (2017). doi:10.2514/1.C034000
24. Welch, P. D.: The use of fast fourier transform for the estimation of power spectra: a method based on time averaging over short. Modified Periodograms. IEEE Trans. Audio Electroacoust. **15**(2), 70–73 (1967). doi:10.1109/TAU.1967.1161901
25. Liu, X., Thomas, F. O., Nelson, R. C.: An experimental investigation of the planar turbulent wake in constant pressure gradient. Phys. Fluids **14**(8), 2817–2838 (2002). doi:10.1063/1.1490349
26. Amiet, R. K.: Compressibility effects in unsteady thin-airfoil theory. AIAA J. **12**(2), 252–255 (1974). doi:10.2514/3.49212
27. Heidelberg, L. J., Woodward, R. P.: Advanced turboprop wing installation effects measured by unsteady blade pressure and noise. AIAA 11th Aeroacoustics Conference, Palo Alto, CA, USA (1987). doi:10.2514/6.1987-2719
28. Veldhuis, L. L. M.: Propeller wing aerodynamic interference. Ph.D. Thesis, Delft University of Technology, Delft, The Netherlands (2005)
29. Hanson, D. B.: Sound from a propeller at angle of attack: a new theoretical viewpoint. Proc. R. Soc. Lond. **449**(1936), 315–328 (1995). doi:10.1098/rspa.1995.0046